Molecular Plant
Research Article

CellPress
Partner Journal

A crosstalk between auxin and brassinosteroid regulates leaf shape by modulating growth anisotropy

Yuanyuan Xiong[1,2,7], Binbin Wu[1,2,6,7], Fei Du[1,7], Xiaolu Guo[3], Caihuan Tian[1], Jinrong Hu[4,5], Shouqin Lü[4,5], Mian Long[4,5], Lei Zhang[3,*], Ying Wang[2,*] and Yuling Jiao[1,2,*]

[1]State Key Laboratory of Plant Genomics and National Center for Plant Gene Research (Beijing), Institute of Genetics and Developmental Biology, the Innovative Academy of Seed Design, Chinese Academy of Sciences, Beijing 100101, China

[2]College of Life Sciences, University of Chinese Academy of Sciences, Beijing 100049, China

[3]Beijing International Center for Mathematical Research, Peking University, Beijing 100871, China

[4]Key Laboratory of Microgravity (National Microgravity Laboratory), Center of Biomechanics and Bioengineering, and Beijing Key Laboratory of Engineered Construction and Mechanobiology, Institute of Mechanics, Chinese Academy of Sciences, Beijing 100190, China

[5]School of Engineering Science, University of Chinese Academy of Sciences, Beijing 100049, China

[6]Present address: Baqiao Municipal Health Commission, Xi'an, Shaanxi 710038, China

[7]These authors contributed equally to this article.

***Correspondence: Lei Zhang (zhangl@math.pku.edu.cn), Ying Wang (yingwang@ucas.edu.cn), Yuling Jiao (yljiao@genetics.ac.cn)**

https://doi.org/10.1016/j.molp.2021.03.011

ABSTRACT

Leaf shape is highly variable within and among plant species, ranging from slender to oval shaped. This is largely determined by the proximodistal axis of growth. However, little is known about how proximal–distal growth is controlled to determine leaf shape. Here, we show that *Arabidopsis* leaf and sepal proximodistal growth is tuned by two phytohormones. Two class A AUXIN RESPONSE FACTORs (ARFs), ARF6 and ARF8, activate the transcription of *DWARF4*, which encodes a key brassinosteroid (BR) biosynthetic enzyme. At the cellular level, the phytohormones promote more directional cell expansion along the proximodistal axis, as well as final cell sizes. BRs promote the demethyl-esterification of cell wall pectins, leading to isotropic in-plane cell wall loosening. Notably, numerical simulation showed that isotropic cell wall loosening could lead to directional cell and organ growth along the proximodistal axis. Taken together, we show that auxin acts through biosynthesis of BRs to determine cell wall mechanics and directional cell growth to generate leaves of variable roundness.

Key words: leaf shape, proximodistal axis, growth anisotropy, mechanical signals, AUXIN RESPONSE FACTOR, brassinosteroids

Xiong Y., Wu B., Du F., Guo X., Tian C., Hu J., Lü S., Long M., Zhang L., Wang Y., and Jiao Y. (2021). A crosstalk between auxin and brassinosteroid regulates leaf shape by modulating growth anisotropy. Mol. Plant. **14**, 949–962.

INTRODUCTION

A fundamental question in biology is to understand how genetic information directs organ shape formation (Coen et al., 2017; Gilmour et al., 2017; Das Gupta and Tsiantis, 2018). The complex 3D organ form emerges from coordinated cell behaviors. Genetic approaches have proven to be very powerful in identifying genes, especially upstream regulatory genes that determine tissue patterning. However, it remains poorly understood how the upstream genetic inputs are translated by cellular effectors to direct cell and organ shaping. It is also unclear how cell behaviors are coordinated to enable tissue-scale organization.

As typical plant organs, plant leaves are an attractive system to address these questions (Du et al., 2018; Kuchen et al., 2012; Malinowski et al., 2011; Runions et al., 2017). After initiation from the shoot apical meristem, leaf primordia develop in three orthogonal axes, including the adaxial–abaxial (also called dorsoventral) axis in the up–down direction, the proximodistal axis in the longitudinal direction, and the mediolateral axis in the middle-to-side direction of the leaf (Figure 1A), to form planar leaves that balance photosynthesis and evapotranspiration. Growth along

Published by the Molecular Plant Shanghai Editorial Office in association with Cell Press, an imprint of Elsevier Inc., on behalf of CSPB and CEMPS, CAS.

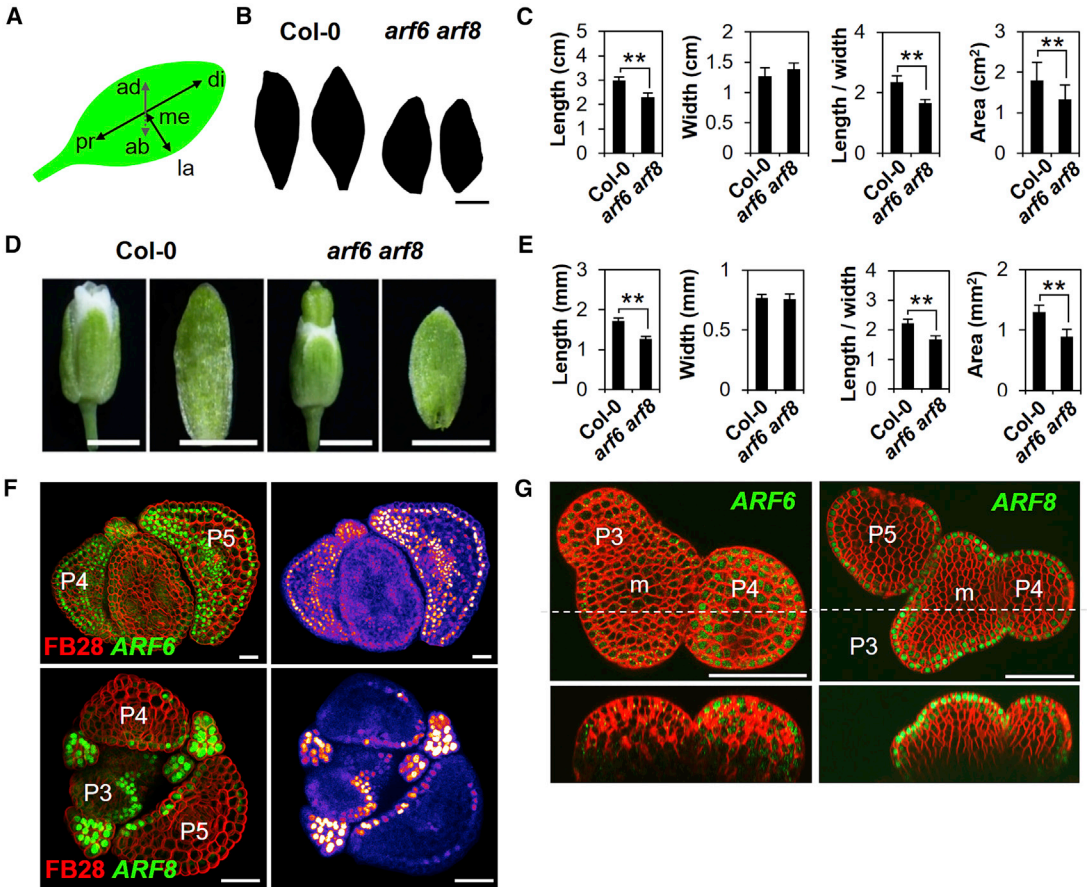

Figure 1. *ARF6* and *ARF8* promote leaf and sepal proximodistal growth.

(A) Schematic of three axes of leaves marked by arrows: proximodistal (pr-di) axis, mediolateral (me-la) axis, and adaxial–abaxial (ad-ab) axis.

(B) Silhouettes of the oldest cauline leaves of Col-0 and *arf6 arf8* plants.

(C) Quantifications of length, width, length–width ratio, and area of cauline leaves shown in **(B)**. Data are presented as mean ± SD for 12 individual plants. $^{**}P < 0.01$ (Student's *t*-test).

(D) Phenotypes of stage 14 flowers and their abaxial sepals of Col-0 and *arf6 arf8* plants.

(E) Quantifications of length, width, length–width ratio, and area of sepals shown in **(D)**. Data are presented as mean ± SD for 12 individual sepals. $^{**}P < 0.01$ (Student's *t*-test).

(F) Agarose transverse sections of leaf primordia stained with FB28 (red) showing *pARF6:n3GFP* (green) and *pARF8:n3GFP* (green) expression. The left panels show confocal images, and the right panels are heatmaps showing GFP signal intensity. P4 and P5 indicate the fourth and fifth youngest primordia, respectively.

(G) Reconstructed optical transverse and longitudinal sections of inflorescence apices stained with FM4-64 (red) showing *pARF6:n3GFP* (green) and *pARF8:n3GFP* (green) expression. The planes of longitudinal sections are depicted by white dotted lines. m, meristem. Scale bars correspond to 1 cm **(B)**, 1 mm **(D)**, 25 μm **(F)**, and 50 μm **(G)**.

the adaxial–abaxial, proximodistal, and mediolateral axes determines the thickness, length, and width of leaves, respectively. Whereas growth in the adaxial–abaxial axis is usually conserved (Zhao et al., 2020), the balance between the proximodistal and mediolateral axes is highly divergent between and within species, resulting in dazzlingly variable leaf shapes. By modulating growth along these two axes, a range of leaf shapes can be obtained, such as linear, oblong, elliptical, and orbiculate. On top of that, further elaborations can generate a wider spectrum of leaf morphology, such as serrations, lobes and leaflets. Many other leaf-like organs, such as sepals, share similar developmental programs. Sepals are initiated from the floral meristem and develop into a leaf-like form. Despite the difference in cell shape, cell size, and organ size, leaves and sepals share many similarities in form acquisition, and are regulated by shared gene regulatory networks. For example, *ASYMMETRIC LEAVES1* mutations result in reduced growth along the proximodistal axis in both leaves and sepals (Sun et al., 2002).

Recent theoretical and experimental work showed how patterning and growth along leaf margins generate serrations, lobes, and leaflets in simple and compound leaves (Runions et al., 2017; Kierzkowski et al., 2019). On the other hand, we know much less about how proximodistal and mediolateral growth rates are balanced. Computational modeling has shown that varying growth along these two axes would lead to leaf shapes ranging from obcordate to ovate and elliptical (Kuchen et al., 2012; Runions et al., 2017). The biochemical and biophysical mechanisms underlying these theoretical models are urgently demanded.

The phytohormone auxin plays a significant role in leaf initiation at the shoot apical meristem periphery (Reinhardt et al., 2000, 2003; Shi and Vernoux, 2019). Two class A AUXIN RESPONSE FACTORs (ARFs), MONOPTEROS (MP) and NONPHOTOTROPIC HYPOCOTYL4, mediate the adaxial–abaxial polarity-dependent mediolateral growth (Guan et al., 2017). These ARFs are activated along the leaf margin to promote blade formation. Moreover, the leaf margin auxin activity can be discontinuous. The interaction between polar auxin transport and the expression of CUP-SHAPED COTYLEDON2 transcription factor forms interspersed auxin activity peaks, which form marginal protrusions or leaflets (Bilsborough et al., 2011; Ben-Gera et al., 2012).

In this study, we show that auxin signaling also contributes to the promotion of proximodistal growth, and that this is mediated by brassinosteroid (BR) biosynthesis and signaling. Two additional class A ARFs activate the expression of a key BR biosynthesis gene to promote BR biosynthesis in the leaf epidermis layer. BR modulates cell wall pectin methyl-esterification and wall mechanics, which is expected to be isotropic. Notably, computational modeling revealed that modulating isotropic wall mechanics may lead to directional cellular and organ growth in leaves and sepals. Thus, phytohormone signals that lack subcellular resolution may direct anisotropic cellular, and organ growth.

RESULTS

ARF6 and ARF8 promote proximodistal growth

To study the roles of auxin in leaf morphology, we analyzed mutants of class A *ARF* genes (Guilfoyle and Hagen, 2007), and found that leaves and leaf-like organs of *arf6 arf8* plants were more rounded than comparably staged wild-type plant organs (Figure 1B–1E). This change was more obvious in cauline leaves and sepals. Whereas leaves and sepals of *arf6 arf8* plants had comparable widths as the wild type, their lengths were significantly reduced (Figure 1B–1E). Total leaf and sepal area was also reduced for *arf6 arf8* (Figure 1C and 1E).

By using *in situ* hybridization, we found that *ARF6* was enriched in the adaxial domain of young leaf primordia (P4 leaf primordium in Supplemental Figure 1) but was ubiquitously expressed in older leaf primordia (P6 leaf primordium in Supplemental Figure 1), and that *ARF8* was mainly enriched in the epidermis and adaxial domain of P4 and P6 leaf primordia (Supplemental Figure 1). Through analyzing expression patterns of *ARF6* and *ARF8* fluorescence reporters, we found that *ARF6* was enriched in the epidermis and adaxial domain of P4 and P5 leaf primordia, and that *ARF8* was specifically expressed in the epidermis of P3–P5 leaf primordia (Figure 1F). In addition, strong signals were found in stipules for both genes (Figure 1F). *ARF8* was also enriched in the floral primordium epidermis, whereas *ARF6* was enriched in the epidermis of young floral primordia but was also expressed in the inner cells of older floral primordia (Figure 1G). Since epidermal restriction plays an important role in organ shape determination (Kutschera and Niklas, 2007; Boudon et al., 2015; Qi et al., 2017; Zhou et al., 2020), we speculate that epidermal auxin signaling mediated by *ARF6* and *ARF8* affects proximodistal growth.

DWF4 mediates proximodistal growth

To understand the downstream effects of epidermal auxin signaling, we searched for publicly available auxin-responsive and epidermal-specific datasets (Goda et al., 2008; Tian et al., 2019). *DWARF4* (*DWF4*), encoding a key enzyme in BR biosynthesis (Choe et al., 1998), is both auxin activated and epidermal enriched. Consistent with previous reports (Azpiroz et al., 1998; Reinhardt et al., 2007), *dwf4* mutant plants had substantially reduced proximodistal growth (Figure 2). Homozygous plants for the E1439 allele lack *DWF4* transcripts and have an intermediate proximodistal growth reduction in cauline leaves and sepals (Figure 2 and Supplemental Figure 2). The *dwf4-102* allele expresses truncated *DWF4* transcripts (Supplemental Figure 2), completely lacks cauline leaves, and has a dramatic reduction in the proximodistal growth and the total area of sepals (Figure 2C and 2D). Consistently, overexpressing *DWF4* led to increased proximodistal growth, both in cauline leaves and sepals, and increased total area in cauline leaves (Figure 2).

To test whether auxin signaling can activate *DWF4* expression, we treated shoot tissues with the auxin analog 2,4-dichlorophenoxyacetic acid (2,4-D). Quantitative reverse-transcription PCR (qRT–PCR) analysis indicated that a 2 h 2,4-D treatment rapidly activated the expression of *GFP* in an auxin-responsive *pDR5*::*NLS-GFP* reporter line, even in the presence of the protein synthesis inhibitor cycloheximide (CHX) (Figure 3A). 2,4-D treatment also rapidly activated *DWF4* expression in the presence of CHX (Figure 3B), suggesting that activation of *DWF4* does not require *de novo* protein synthesis. In addition, *DWF4* expression was significantly reduced in *arf6 arf8* shoot tissues (Figure 3C), suggesting that these two ARF activators play leading roles in activating *DWF4* expression. Consistently, the expression of *DWF4* was detected mostly in the epidermis of leaf and floral primordia (Figure 3E–3G), and significantly overlaps with expression patterns of *ARF6* and *ARF8* (Figures 1F and 1G; Supplemental Figure 1). RNA *in situ* hybridization revealed reduced *DWF4* expression in the epidermis of *arf6 arf8* sepal primordia (Figure 3H), consistent with a significant reduction of *DWF4* transcript in *arf6 arf8* inflorescence apices shown by qRT–PCR (Figure 3D).

The *DWF4* promoter region contains two auxin response element (AuxRE) core motifs, a canonical and a non-canonical AuxRE, the latter one is sufficient for ARF7 recruitment (Chung et al., 2011). To investigate whether the ARF6 and ARF8 proteins directly induce *DWF4* expression, we employed transient expression assays in *Arabidopsis* leaf protoplasts to test the effects of ARF6 and ARF8 on *pDWF4*::*firefly luciferase* (*Luc*) reporter expression. We constructed constitutively active truncated proteins of ARF6 and ARF8 that lack domains III and IV. The truncated proteins, termed ARF6Δ and ARF8Δ, are predicted to escape the negative regulation conferred by repressive Aux/IAA binding partners (Krogan et al., 2012). We observed that both ARF6Δ and ARF8Δ promoted expression of *pDWF4*::*Luc* (Figure 3I). In addition, we performed a yeast one-hybrid assay and found that ARF6 could bind to the promoter fragment of *DWF4* containing the canonical AuxRE motif but not the non-canonical motif containing fragment, while ARF8 could not bind to either the canonical or the non-canonical AuxRE

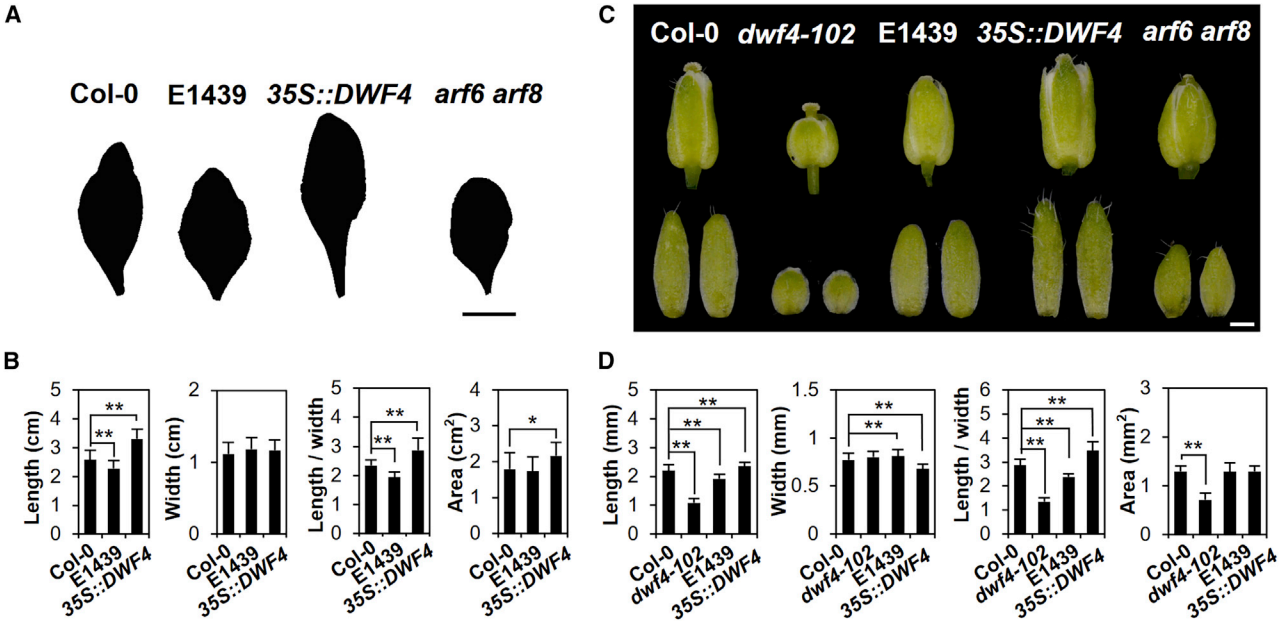

Figure 2. *DWF4* promotes leaf and sepal proximodistal growth.

(A) Silhouettes of the oldest cauline leaves of Col-0, E1439, *35S*:*DWF4*, and *arf6 arf8* plants.

(B) Quantifications of length, width, length–width ratio, and area of cauline leaves shown in **(A)**. Data are presented as mean ± SD for more than 12 individual plants. $^{*}P < 0.05$, $^{**}P < 0.01$ (Student's *t*-test).

(C) Phenotypes of stage 13 flowers and their abaxial sepals of Col-0, *dwf4-102*, E1439, *35S*::*DWF4*, and *arf6 arf8* plants.

(D) Quantifications of length, width, length–width ratio, and area of sepals shown in **(C)**. Data are presented as mean ± SD for more than 12 individual sepals. $^{**}P < 0.01$ (Student's *t*-test). Scale bars correspond to 1 cm **(A)** and 0.5 mm **(C)**.

motif-containing fragment (Figure 3J and 3K). Taken together, our data indicated that *DWF4* expression is directly activated by ARF6 and directly or indirectly activated by ARF8. Furthermore, the bound motif by ARF6 is different from that by ARF7 (Chung et al., 2011).

To test whether the reduction of *DWF4* expression accounts for the reduced proximodistal growth in *arf6 arf8* plants, we applied 24-epibrassinolide (EBL) to *arf6 arf8* inflorescence apices and found significant restoration of proximodistal growth in sepals (Figure 3L and 3M). Moreover, the degree of restoration is positively correlated with the EBL concentration.

Taken together, our data indicate that an auxin–BR crosstalk promotes leaf proximodistal growth. This would predicate that BR signaling modulates leaf shape. Indeed, we observed similar proximodistal growth reduction in mutants defective in BR signaling (Figure 4) (Pérez-Pérez et al., 2002; Wang et al., 2018), although it is unknown how BR signaling promotes directional growth.

The phytohormone crosstalk changes cell geometry

To uncover how auxin and BR guide cell growth and further directional organ growth, we measured abaxial cauline leaf and sepal epidermal cell geometry (Figure 5A–5F). We observed that *arf6 arf8* leaf pavement cells were shorter in the proximodistal direction, but slightly wider in the mediolateral direction (Figure 5A and 5B). Sepal epidermal cells from *arf6 arf8* were shorter in the proximodistal direction than wild-type cells but had comparable width in the mediolateral direction (Figure 5C and 5D). *dwf4-102* sepal epidermal cells showed a similar reduction of growth in the proximodistal direction (Figure 5E and 5F). We found comparable cell numbers along the proximodistal direction among Columbia-0 (Col-0), *arf6 arf8*, *dwf4-102*, E1439, and *35S*::*DWF4* sepals (Supplemental Figure 3A–3C), suggesting that the phytohormone crosstalk does not affect cell division. Of note, the number of giant cells was reduced in *dwf4-102* sepals (Supplemental Figure 3A and 3D).

We further performed time-lapse imaging to better understand the details of cell growth (Figure 5G–5I). Using MorphoGraphX (Barbier de Reuille et al., 2015), we segmented abaxial sepal epidermal cells for two time points at 12 h intervals and analyzed their growth properties. We measured the ratio of cell deformation in the maximal direction to the minimal direction during the growth interval, and referred to this as "growth anisotropy." Since sepals at early stages are undergoing high anisotropic growth along the proximodistal direction (Hervieux et al., 2016), growth anisotropy is taken as the change of proximodistal/mediolateral length ratio. Growth anisotropy includes both growth direction and growth rate along each axis, and these parameters may simultaneously change. We also measured cell growth rate as the change of cell size over time. We observed that cell growth rate was lower, and cell size was smaller in E1439 and *dwf4-102* (Figure 5G–5I). Furthermore, cell growth anisotropy in E1439 and *dwf4-102* was also substantially reduced compared with controls (Figure 5G and 5I), which is consistent with directional sepal growth along the proximodistal axis.

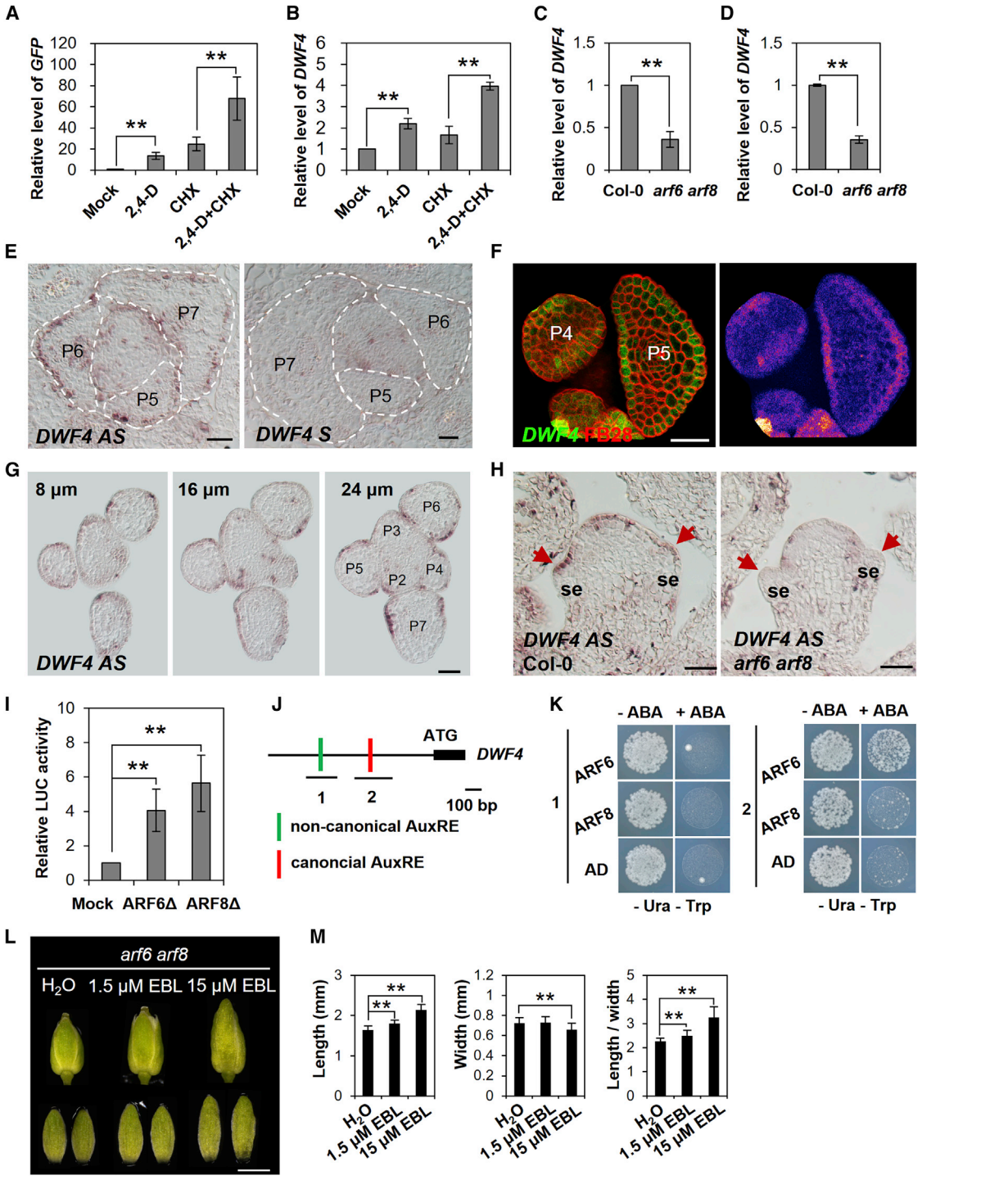

Figure 3. ARF6 and ARF8 directly activate the expression of *DWF4*.

(A) qRT–PCR analysis of *GFP* expression in *pDR5*::*NLS-GFP* rosette leaves after 2 h 2,4-D, CHX treatment, and their co-treatment. Data are presented as mean ± SD for three independent experiments. $^{**}P < 0.01$ (Student's *t*-test).

(B) qRT–PCR analysis of *DWF4* expression in Col-0 rosette leaves after 2 h 2,4-D, CHX treatment, and their co-treatment. Data are presented as mean ± SD for three independent experiments. $^{**}P < 0.01$ (Student's *t*-test).

(C and D) qRT–PCR analysis of *DWF4* expression in Col-0 and *arf6 arf8* seedlings **(C)** and inflorescence **(D)**. Data are presented as mean ± SD for three independent experiments. $^{**}P < 0.01$ (Student's *t*-test).

(E) The pattern of *DWF4* transcript accumulation in transverse sections of leaf primordia of a Col-0 plant. AS, antisense probe; S, sense probe.

(F) A transverse section of leaf primordia of a heterozygous E1439 plant stained with FB28 (red) showing *DWF4* (green) expression. The left panel shows a confocal image, and the right panel is a heatmap showing GFP signal intensity.

(legend continued on next page)

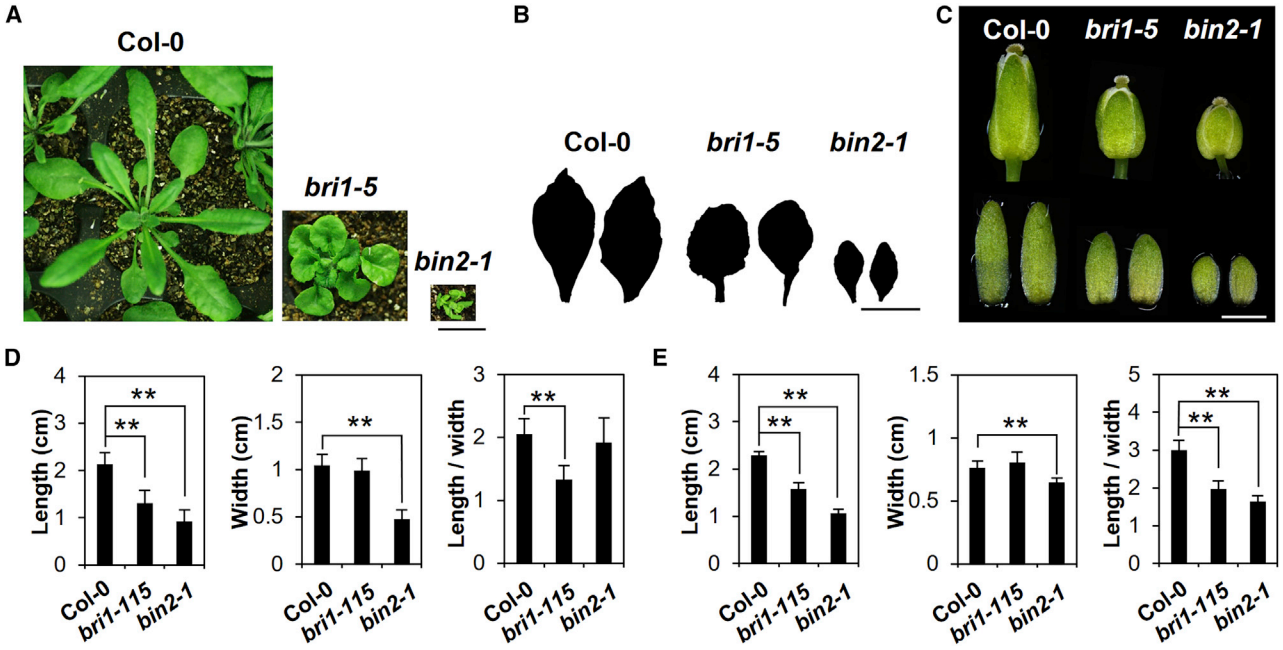

Figure 4. BR signaling determines leaf and sepal proximodistal growth.

(A) Vegetative phenotypes of 1-month-old Col-0, *bri1-5*, and *bin2-1* plants.

(B) Silhouettes of the oldest cauline leaves of Col-0, *bri1-5*, and *bin2-1* plants.

(C) Phenotypes of stage 13 flowers and their abaxial sepals of Col-0, *bri1-5*, and *bin2-1* plants.

(D) Quantifications of length, width, and length–width ratio for cauline leaves shown in **(B)**. Data are presented as mean ± SD for more than 12 individual plants. $^{**}P < 0.01$ (Student's *t*-test).

(E) Quantifications of length, width, and length–width ratio for sepals shown in **(C)**. Data are presented as mean ± SD for more than 12 individual sepals. $^{**}P < 0.01$ (Student's *t*-test). Scale bars correspond to 1 cm **(A and B)** and 1 mm **(C)**.

The phytohormone crosstalk regulates pectin demethyl-esterification and reduces wall elasticity

Cell wall mechanics strongly influence cell growth (Ali et al., 2014; Sampathkumar et al., 2014). In the root, BRs promote demethyl-esterification of pectic homogalacturonan (HG) (Wolf et al., 2012). We used the monoclonal antibody 2F4 and LM19 (Verhertbruggen et al., 2009), which specifically labels low methyl-esterified and demethyl-esterified HG, respectively, to analyze the demethyl-esterification status of HG in sepal cross-sections. We quantified the mean fluorescence levels of 2F4 and LM19 signals in adaxial and abaxial epidermal cells, respectively, and found that 2F4 and LM19 signal intensities were decreased in *dwf4-102* adaxial epidermal cells, and that 2F4 signal intensity was also decreased in *dwf4-102* abaxial epidermal cells (Figure 6A–6C and Supplemental Figure 4), suggesting that BRs promote HG demethyl-esterification in sepals as in roots.

HG demethyl-esterification changes multiple facets of wall mechanics. Tensile stretching assays show that HG demethyl-esterification increases wall plasticity, which is expected to be isotropic in-plane (Wang et al., 2020). At the same time, nanoindentation assays indicate that HG demethyl-esterification reduces elastic modulus normal to the wall surface (Peaucelle et al., 2011; Wang et al., 2020). As it is impossible to isolate sepal walls for tensile stretching assays, we performed atomic force microscopy (AFM)-based nanoindentation assays to measure the elastic modulus of the abaxial epidermal cell wall in living cauline leaves and sepals (Figure 6D and 6E; Supplemental Figure 5). We randomly selected multiple cells

(G) The pattern of *DWF4* transcript accumulation in a series of transverse section through an inflorescence apex of Col-0 plant.

(H) Comparison of *DWF4* transcript accumulation in longitudinal sections of the stage 3 flower sepals of Col-0 and *arf6 arf8* plants through *in situ* hybridization. Note the decrease of expression levels in *arf6 arf8* sepals, shown by the red arrows. se, sepal.

(I) The relative activity of *pDWF4*::*LUC* induced by ARF6Δ and ARF8Δ in protoplast, normalized by the mock. Data are presented as mean ± SD for three independent experiments. $^{**}P < 0.01$ (Student's *t*-test).

(J) Schematic of the 1 kb promoter of the *DWF4* gene. The green box indicates a non-canonical AuxRE (5′-TGTGCTC-3′, -683 ~ -689) site, and the red box indicates a canonical AuxRE (5′-TGTCTC-3′, -381 ~ -386) site. The underlying lines represent the DNA fragments used for Y1H assay.

(K) Y1H assay of *DWF4* genomic fragments shown in **(J)** with ARF6, ARF8, or AD (pDEST22) plasmid as control.

(L) Phenotypes of stage 13 flowers and their abaxial sepals of *arf6 arf8* after treatment with 1.5 μM 24-epibrassinolide (EBL), 15 μM EBL, or water as control.

(M) Quantifications of length, width, and length–width ratio of sepals shown in **(L)**. Data are presented as mean ± SD for 12 individual sepals. $^{**}P < 0.01$ (Student's *t*-test). Scale bars correspond to 25 μm **(E–H)** and 1 mm **(L)**.

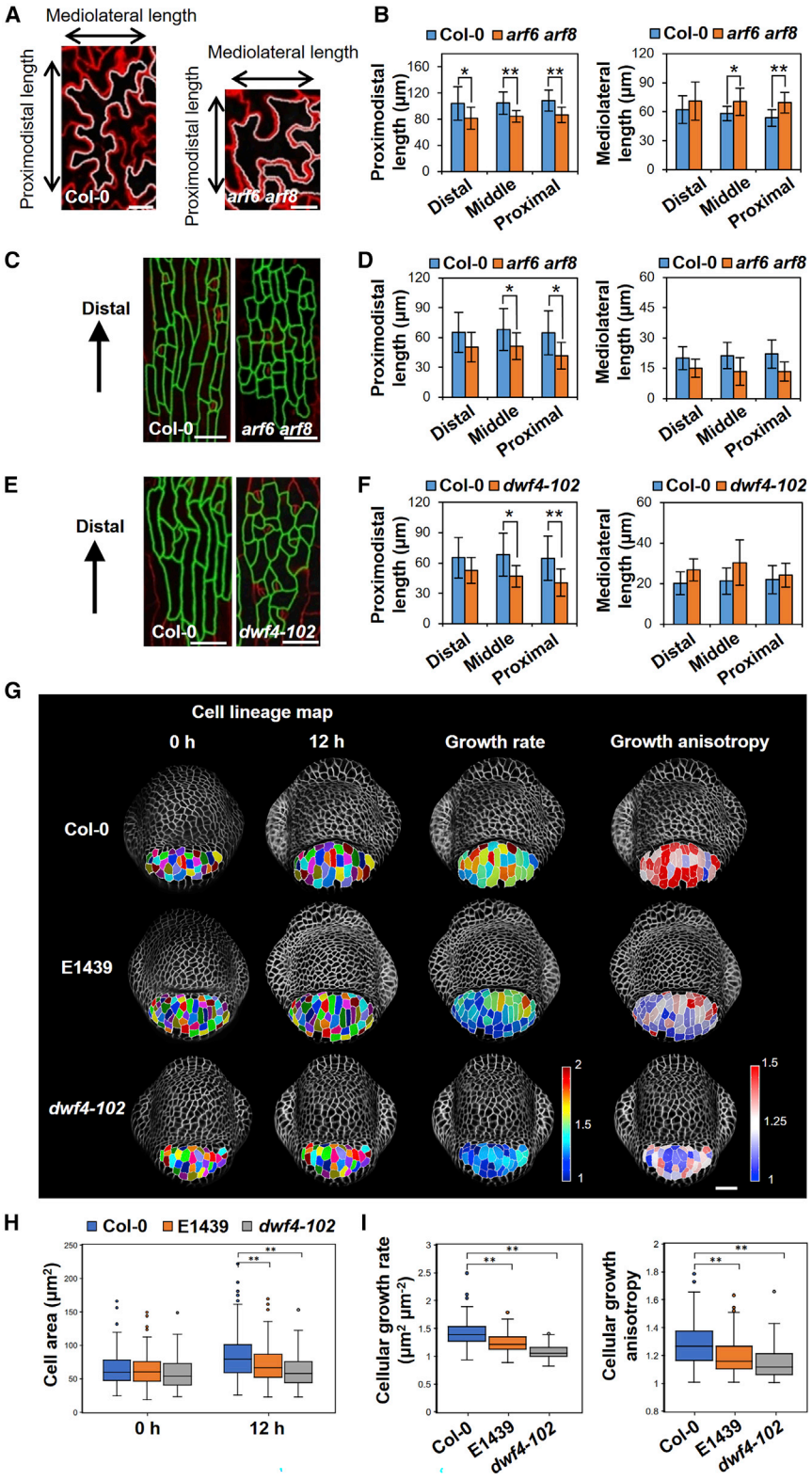

Figure 5. The phytohormone crosstalk modulates anisotropic cell growth.

(A) Morphologies of abaxial epidermal cells of the oldest cauline leaves of Col-0 and *arf6 arf8* plants.

(B) Quantifications of cell lengths of cauline leaves shown in **(A)** along proximodistal and mediolateral axes, respectively. Distal, middle, and proximal regions were separately quantified. Data are presented as mean ± SD for the average value from 20 cells of a plant; 10 individual plants were used for quantification. **P* < 0.05, ***P* < 0.01 (Student's *t*-test).

(C) Morphologies of abaxial epidermal cells of stage 14 flower sepals of Col-0 and *arf6 arf8* plants.

(D) Quantifications of cell lengths of sepals shown in **(C)** along proximodistal and mediolateral axes, respectively. Distal, middle, and proximal regions were separately quantified. Data are presented as mean ± SD for the average value from 20 cells of a sepal; 10 individual sepals were used for quantification. **P* < 0.05 (Student's *t*-test).

(E) Morphologies of abaxial epidermal cells of stage 14 flower sepals of Col-0 and *dwf4-102* plants.

(F) Quantifications of cell lengths of sepals shown in **(E)** along proximodistal and mediolateral axes, respectively. Distal, middle, and proximal regions were separately quantified. Data are presented as mean ± SD for the average value from 20 cells of a sepal, 10 individual sepals are used for quantification. **P* < 0.05, ***P* < 0.01 (Student's *t*-test).

(G) Heatmaps of cellular growth rate and cellular growth anisotropy quantified based on cell lineage maps for abaxial sepal cells of stage 3 flowers of Col-0, E1439, and *dwf4-102* plants.

(H) Quantifications of cell area for sepals shown in **(G)**. Each data column is displayed in boxplots. ***P* < 0.01 (Student's *t*-test).

(I) Quantifications of cellular growth rate and cellular growth anisotropy for sepals shown in **(G)**. The cellular growth rate was calculated as the ratio of cell area in the corresponding growth interval. Cellular growth anisotropy is calculated as the ratio of cell deformation in the maximal direction to the minimal direction in the corresponding growth interval. Each data column is displayed in boxplots. ***P* < 0.01 (Student's *t*-test). Scale bars correspond to 25 μm **(A)**, 50 μm **(C and E)**, and 20 μm **(G)**.

within each spatial domain from wild-type, *arf6 arf8*, E1439, and *35S::DWF4* leaves and from the middle domain of their sepals. The strong *dwf4-102* allele lacks cauline leaves and its sepals are too small to perform reliable AFM measurements. By quantitatively comparing the elastic moduli of epidermal cell walls from comparable regions without vertical (anticlinal) cell walls below, we found that *arf6 arf8* and E1439 leaves and sepals had higher elastic moduli than wild type, and *35S::DWF4* leaves and sepals had a lower elastic modulus (Figure 6D and 6E; Supplemental Figure 5). Although the indentation modulus of the weak E1439 allele and *35S::DWF4* sepals and leaves are significantly different from the wild type, we could not detect significant differences in fluorescence intensity by LM19 immunolabeling, likely due to its low sensitivity.

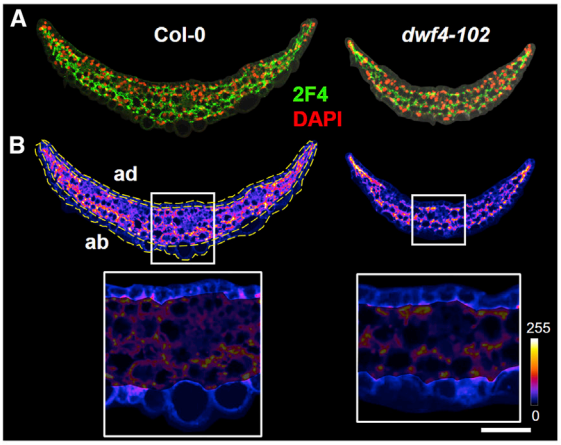

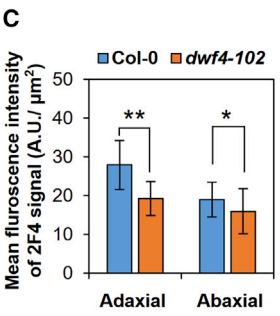

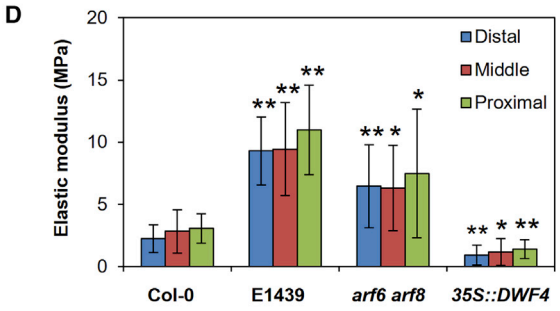

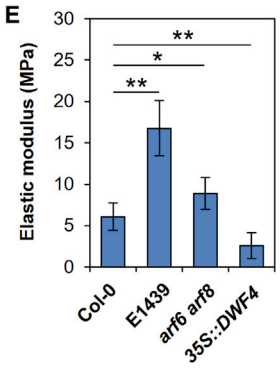

Figure 6. The phytohormone crosstalk regulates pectin demethyl-esterification and wall elasticity.

(A) Transverse sections through sepals of stage 8 flowers of Col-0 and *dwf4-102* plants stained with DAPI (red) showing 2F4 labeling (green) of low methyl-esterification HG.

(B) Heatmaps of 2F4 signal intensity in **(A)**. ad, adaxial side; ab, abaxial side. The yellow dotted lines indicate the epidermal cells used for quantitative analysis of 2F4 signal intensity.

(C) Quantitative analysis of 2F4 signal intensity in **(B)**. Data are presented as mean ± SD for more than 12 individual sepals. $^{*}P < 0.05$, $^{**}P < 0.01$ (Student's *t*-test).

(D) Quantifications of the apparent Young's modulus of epidermal cells obtained by AFM for distal, middle, and proximal regions of cauline leaves of Col-0, E1439, *arf6 arf8*, and *35S::DWF4* plants. A total of 10 cells in five leaf samples were recorded per region for each plant, with epidermal cell topography and elasticity provided in Supplemental Figure 5A. Data are presented as mean ± SD. $^{*}P < 0.05$, $^{**}P < 0.01$ (Student's *t*-test).

(E) Quantifications of the apparent Young's modulus of epidermal cells obtained by AFM for middle region of sepals of Col-0, E1439, *arf6 arf8*, and *35S::DWF4* plants. A total of five cells in five sepal samples were recorded for each plant, with epidermal cell topography and elasticity provided in Supplemental Figure 5B. Data are presented as mean ± SD. $^{*}P < 0.05$, $^{**}P < 0.01$ (Student's *t*-test).

Scale bar corresponds to 50 μm.

Modulating isotropic wall mechanics may affect directional growth

The above chain of molecular events suggests that a crosstalk of phytohormones regulates in-plane isotropic wall mechanics. How do wall mechanics regulate directional cell and organ growth? To this end, computational modeling offers a way to understand growth and geometry (Roeder et al., 2011; Ali et al., 2014; Runions et al., 2017; Whitewoods and Coen, 2017).

Plant cell growth is determined by the balance between turgor pressure and wall restriction. Whereas turgor pressure is uniform and isotropic, anisotropic wall restriction leads to asymmetric cell growth (Ali et al., 2014; Sampathkumar et al., 2014). The orientation of the rigid cellulose microfibrils commonly provides directional restrictions to wall expansion. The pattern of cellulose microfibrils relies on cortical microtubule (CMT) orientation (Paredez et al., 2006). In sepals, CMTs generally align more in the mediolateral direction, as shown by the MBD-GFP reporter (Hervieux et al., 2016). We observed comparable MBD-GFP alignment in *35S::DWF4* sepals (Supplemental Figure 6). These observations are consistent with stronger restriction of expansion along the mediolateral direction, and more expansion along the proximodistal direction.

We first developed a cell growth model to describe cell shape changes resulting from the balance between turgor and wall restriction. The wall was set to be anisotropic, and the elasticity matrix was split into two parts: one isotropic, and the other anisotropic in a fixed direction. The former part represents mechanical restriction derived from pectin, hemicellulose, and isotropically aligned cellulose, whereas the latter part corresponds to anisotropic cellulose microfibrils. To model growth, we treated the elastic and plastic regimes separately and modeled growth incrementally. Based on turgor pressure and wall elasticity, we computed the equilibrium shape of each step, which provides the initial shape for the following step. Turgor is then applied again in the subsequent step (see Supplemental information for more details).

Based on experimental observations, we fixed anisotropic wall restriction, and altered the levels of isotropic wall restriction to recapitulate different levels of elastic modulus in each genotype. By altering isotropic wall restriction, we obtained different levels of directional cell growth (Figure 7A and 7B). When the isotropic wall restriction is increased, we obtained reduced growth anisotropy and growth rate, mimicking the *dwf4* mutants. Consistently, reducing the isotropic wall restriction resulted in more anisotropic growth and increased growth rate, mimicking *35S::DWF4* cells.

We next modeled sepal and leaf growth using a finite element method that accounts for the outer epidermal walls as a continuous two-dimensional surface (Hervieux et al., 2016). Starting with a semicircular shape, a primordium is under uniform turgor pressure. After the maturation gradient (Andriankaja et al., 2012; Hervieux et al., 2016; Kuchen et al., 2012), we assigned

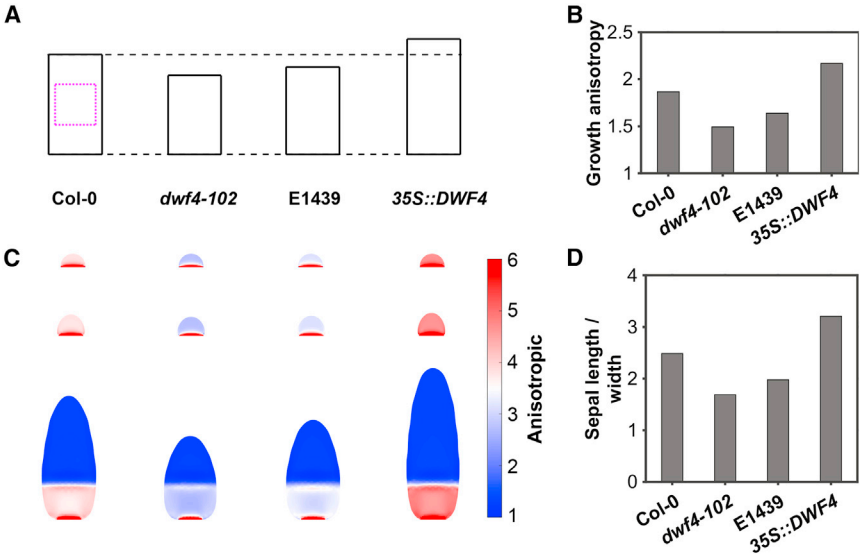

Figure 7. Isotropic wall biomechanical property may influence cell and organ growth anisotropy.

(A) Cell directional growth model results of Col-0, *dwf4-102*, E1439, and *35S*::*DWF4* plants. The magenta dotted line indicates the original shape of the cell (square), and the black solid line indicates the cell shape after growth.

(B) The predicted cell growth anisotropy in Col-0, *dwf4-102*, E1439, and *35S*::*DWF4* plants.

(C) Sepal growth simulation results of Col-0, *dwf4-102*, E1439, and *35S*::*DWF4* plants. The first row represents the original shape (half-circle) of the sepal; the second row represents the early extension of the sepal; the third row represents the late-stage shape. The heatmap shows the growth anisotropy in different types and different stages of the plants.

(D) The predicted length–width ratio for the late-stage sepals of Col-0, *dwf4-102*, E1439, and *35S*::*DWF4* plants.

the elastic modulus to increase along the proximodistal axis with the tip having the highest value. On top of that, we applied a directional wall restriction in the mediolateral direction. Wall mechanics and growth were described similarly to the above model. This model reproduces early sepal development (Figure 7C and 7D), including the sharp decay in growth rate (Hervieux et al., 2016; Fox et al., 2018).

When we altered the isotropic wall restriction, we obtained sepals with different levels of proximodistal growth (Figure 7C and 7D). The model predictions were well lined with the experiments, and revealed a nonlinear negative relationship between the length/width ratio of a cell and its isotropic wall elastic modulus (Supplemental Figure 7), which is inferred from the underlying elastodynamics simulations. When the isotropic wall restriction was increased, we obtained reduced proximodistal growth, mimicking *dwf4* and BR signaling mutants. Consistently, reducing isotropic wall restriction resulted in extended proximodistal growth, mimicking the growth pattern of *35S*::*DWF4* plants. In contrast, mediolateral growth was only mildly affected. Through sensitivity analysis, we showed that our model conclusion is robust in the reasonable parameter space (Supplemental Figure 7B).

DISCUSSION

Plant organ morphogenesis arises from coordinated changes in cell shape determined by cell wall mechanics and subsequent wall restriction. Patterns of gene expression define cell behaviors in part by controlling cell wall biomechanics. We investigate how a transcriptional regulation connecting two phytohormone pathways influences the orientation of cell growth to generate different leaf shapes. To this end, we combined molecular and genetic studies with cellular-level growth and mechanical data. Coupled with theoretical modeling, we showed that auxin and BRs isotropically influence wall mechanical properties, which remarkably translates into directional cell and organ growth to determine leaf roundness.

At the level of gene regulation, we found that two class A ARFs, *ARF6* and *ARF8*, were expressed mainly in the epidermis. As part of the auxin signaling pathway, ARF6 and ARF8 promote proximodistal growth in leaves and sepals. By contrast, MP, a related class A ARF, activates *WOX* gene expression in internal cells, which promotes mediolateral growth (Guan et al., 2017). The expression patterns of *MP* and *ARF6*/*ARF8* are largely complementary. We further showed that ARF6 and ARF8 promote the expression of the BR biosynthetic gene *DWF4* through direct or indirect binding to its promoter region. Like *ARF6* and *ARF8*, the *DWF4* transcript is also enriched in the epidermis. Thus, epidermal BR signaling is downstream of auxin to promote proximodistal growth. This model is in line with the proposal that epidermal restriction plays an important role in organ shape determination (Kutschera and Niklas, 2007; Boudon et al., 2015; Qi et al., 2017; Zhou et al., 2020). Note that the phenotype of *arf6 arf8* leaves is milder than that of the strong *dwf4-102* allele, suggesting the potential involvement of additional *ARF* genes and other genes in regulating *DWF4* expression.

At the cellular effectors level, our data showed that the auxin and BR crosstalk promoted HG demethyl-esterification in sepals and leaves, as in other organs and tissues (Wolf et al., 2012; Braybrook and Peaucelle, 2013). This regulation provides a link between upstream regulatory genes and signaling molecules to downstream cellular effectors. We found that HG demethyl-esterification correlates with reduced cell wall nanoscale indentation elastic modulus as measured by AFM. This is likely associated with increases in isotropic in-plane wall plasticity (Wang et al., 2020). Our theoretical analysis explained why modulating the isotropic wall mechanical property can result in directional cell and organ growth. Together with a reduction in growth anisotropy, cell growth, i.e., the change of cell size, is also reduced in the mutants and shown by simulations. As mentioned earlier, these parameters are interconnected. For an anisotropically growing cell, more growth would further increase the anisotropy of cell shape. Auxin and BR promote proximodistal growth more than mediolateral growth, leading to increased growth anisotropy and growth rate in general.

Leaf roundness is an important factor affecting adaptation to the environment. Previous work showed that modulating a mechanical

feedback mechanism can change leaf shape roundness (Hervieux et al., 2016). Our findings provide a remarkable example in which modulating isotropic wall mechanical properties can also impact directional growth. Change of leaf roundness is a classical BR signaling phenotype, although the underlying mechanism remains unknown. Our findings explain why BR signaling, whose components are usually isotropic at the subcellular level, can regulate directional cell and organ growth.

METHODS

Growth conditions

Arabidopsis thaliana plants were grown on soil in a growth chamber under constant light at 22°C. For phenotype observation of cauline leaves and sepals, plants were grown under constant light conditions until they had three to five siliques. For gene expression analysis in leaves, plants were grown under short-day conditions (8 h light/16 h dark) for 15 days before *in situ* hybridization or low-melting agarose sectioning.

Genetic material

The *Arabidopsis thaliana* ecotype Col-0 was used as the wild type. The *arf6-1 arf8-2* (CS24632) (Okushima et al., 2005), E1439 (CS70104) (Reinhardt et al., 2007), *dwf4-102* (SALK_020761) (Nakamoto et al., 2006), *35S*::*DWF4* (Belkhadir et al., 2012), *bin2-1* (Li et al., 2001), *pARF6*::*n3GFP*, *pARF8*::*n3GFP* (Rademacher et al., 2011), and *pDR5*::*NLS-GFP* (De Rybel et al., 2010) are in the Col-0 background. The *bri1-5* mutant is in the Wassilewskija-2 (Ws-2) background (Noguchi et al., 1999). The *35S*::*GFP-MBD* is in the Ws-4 background (Hervieux et al., 2016). *35S*::*DWF4 35S*::*GFP-MBD* was generated by crossing.

Chemical treatment, RT–PCR and qRT–PCR

For 2,4-D treatment, a 1 M stock solution of 2,4-D in DMSO was diluted with $^1/_2$ MS liquid medium to a final concentration of 5 mM. $^1/_2$ MS liquid medium with only DMSO was used as a mock control. For 2,4-D and CHX treatment, a 1 M stock solution of 2,4-D and a 10 mM stock solution of CHX in DMSO were diluted with $^1/_2$ MS liquid medium to a final concentration of 5 mM and 10 μM, respectively. $^1/_2$ MS liquid medium with only DMSO was used as a mock control. Seedlings grown on $^1/_2$ MS medium for 10 days under constant light were soaked in the above treatment solutions.

For EBL treatment, a 1 M stock solution of EBL in ethyl alcohol was diluted with water to a final concentration of 1.5 or 15 μM. Water was used as a mock control. Four-week-old plants under constant light were sprayed three times at 2-day intervals with the above treatment solutions.

Total RNA was extracted from seedlings with roots and cotyledons removed or inflorescences using the AxyPrep Multisource RNA Miniprep Kit (Corning) according to the manufacturer's instructions. The first strand of cDNA was synthesized using the TransScript One-Step gDNA Removal and cDNA Synthesis SuperMix (TransGen Biotech) and then used as the templates for RT–PCR or qRT–PCR. qRT–PCR was performed on a Bio-Rad CFX96 real-time detection system using the KAPA SYBR FAST qPCR kit (Kapa Biosystems). *ACTIN2* (*AT3g18780*) was used as the reference gene to normalize the relative expression for qRT–PCR analysis. The primers used in RT–PCR or qRT–PCR are listed in Supplemental Table 1.

In situ hybridization

The probe for *ARF6* was generated through amplifying nucleotides +1180 to +2370 of the *ARF6* coding sequence with primers oFD119 and oFD120. The probe of *ARF8* was generated through amplifying nucleotides +1138 to +2099 of the *ARF8* coding sequence with primers oFD121 and oFD122. The probe of *DWF4* was generated through amplifying nucleotides +1 to +1068 of the *DWF4* coding sequence with primers oFD123 and oFD124. The PCR fragments were cloned into the pGEM-T Easy vector (Promega) for *in vitro* transcription using the Digoxigenin Labeling Kit (Roche). The long probes were then hydrolyzed to an average length of 150 bp and resuspended in 50% formamide at the desired concentrations. Primers for amplifying probes are listed in Supplemental Table 1.

Nonradioactive *in situ* hybridization was performed on 8 μm paraffin sections cut with a Leica RM2255 rotary microtome as described previously (Zhang et al., 2017). Both the hybridization and washing processes were performed at 55°C, with signal development at room temperature.

Yeast one-hybrid assay

To make the bait constructs for yeast one-hybrid assay, the promoter fragments of *DWF4* were amplified from genomic DNA and inserted into pAbAi vector (Clontech). To make the prey constructs, the coding sequences of *ARF6* and *ARF8* were amplified from cDNA and inserted into the *pDEST22* (Life Technologies) vector, respectively. The primers used for vector construction were listed in Supplemental Table 1.

The bait plasmids were linearized by *Bst*BI restriction enzyme and integrated into yeast strain Y1HGOLD using polyethylene glycol (PEG)-mediated transformation according to the manufacturer's instructions (Yeast Hand Book; Clontech, PT3024-1). After selection on media lacking uracil and verification by PCR using an AbA^r gene-specific primer and a yeast genome-specific primer, bait strains were tested for background AbA^r expression. According to the manufacturer's manual (Matchmaker Gold Yeast One-Hybrid Library Screening System, Clontech, 630491), prey plasmids were directly transformed into bait strains through PEG-mediated transformation, and transformants were selected on media lacking uracil and tryptophan but containing 500 ng/ml aureobasidin A (AbA). An equal amount of transformed yeast culture was plated on medium lacking uracil and tryptophan without addition of AbA to control for transformation efficiency. Positive interactions were identified based on growth ability after transformation on AbA-containing medium for 3 days. All interactions were validated by retesting using the same procedure.

Transient expression in protoplasts

The truncated coding sequences of *ARF6* (2352 bp downstream of the start codon) and *ARF8* (2112 bp downstream of the start codon), termed *ARF6Δ* and *ARF8Δ*, were amplified from *Arabidopsis* cDNA by PCR and inserted into the *pUC19-p35S-FLAG-RBS* vector, respectively (Feng et al., 2012). To generate the *DWF4* promoter-driven *Luc* vector, 1942 bp upstream of the *DWF4* start codon was amplified from *Arabidopsis* genomic DNA. PCR fragments were inserted into the corresponding sites of the *pFRK1*::*Luc* vector (Feng et al., 2012). The primers used for vector construction are listed in Supplemental Table 1.

Isolation of *Arabidopsis* protoplasts and PEG-mediated transfection were performed as described previously (Zhao et al., 2017). The transformation of only the *pDWF4*::*Luc* construct into protoplasts was used for mock control.

Agarose sectioning

For agarose sectioning, seedlings were grown in $^1/_2$ MS medium under short-day conditions for 15 days after seed germination. Seedling roots and cotyledons were removed, collected, and immediately immersed in precooled 2.5% paraformaldehyde (PFA) (Sigma-Aldrich) at pH 7.0, vacuum infiltrated for 30 min at 4°C, and then stored overnight at 4°C. The fixed tissue samples were washed with 10% (w/v) sucrose with 1% PFA at pH 7.0 for 20 min, 20% sucrose with 1% PFA at pH 7.0 for 20 min, and 30% sucrose with 1% PFA at pH 7.0 for 30 min, successively. The samples were then embedded in 6% (w/v) low-melting agarose (Promega) liquid gel at 30°C and placed at 4°C for 15 min to solidify. Sections of 40–50 μm were made using a Leica VT1000S vibratome and then stained with 0.01% Fluorescent Brightener 28 (FB28) (Sigma-Aldrich) for 20 min in

darkness. After three washes in water, sections were examined using a confocal laser scanning microscope as detailed below.

Live imaging

For live imaging of epidermal cell geometry of cauline leaves or sepals, plants were grown under constant light conditions until they had three to five siliques. The oldest cauline leaves and stage 13/14 flower sepals were detached and 10 μg/ml FM4-64 (Thermo Fisher) plus 0.01% (v/v) Silwet-77 (Coolaber) were applied for 10 min. The abaxial side of cauline leaves and sepals were facing upward under coverslips and examined using a confocal laser scanning microscope.

For live imaging of sepals or flowers, we used fine forceps and fine syringe tips to carefully remove siliques and old flowers (older than stage 3) under a stereomicroscope (Nikon, SMZ18). The dissected inflorescence apex was directly imaged (for CMT array imaging) or stained with 10 μg/ml FM4-64 for 10 min on ice before imaging. Live imaging was performed using a 60× water immersion lens. For time-lapse live imaging, the water was discarded and the dissected inflorescence apex was transferred back to the growth medium ($^1/_2$ MS medium with 1% agarose on the top) and cultured *in vitro* for 12 h under long-day conditions before imaging at the next time point. Confocal stacks were acquired at 1024 × 1024-pixel resolution. For accurate curvature analysis (i.e., the analysis of cell growth rate, cell growth anisotropy and CMT array anisotropy in MorphoGraphX), the distance between stacks was set to 0.5 μm.

Optical microscopy, confocal microscopy, and scanning electron microscopy

The optical photographs were taken using a Nikon SMZ1000 stereoscopic microscope or an Olympus BX60 microscope equipped with a Nikon DS-Ri1 camera head. Confocal imaging was performed using a Nikon A1 confocal laser scanning microscope. To detect 4′,6-diamidino-2-phenylindole (DAPI) (Sigma-Aldrich) and FB28 staining, a 405 nm laser line was used for excitation, and emission was collected at 425–475 nm. To detect the GFP signal, a 488 nm laser line was used for excitation, and emission was collected at 500–530 nm. To detect FM4-64 staining, and Alexa Fluor 546 signal, a 561 nm laser line was used for excitation, and emission was collected at 660–740 nm. Scanning electron microscopy was performed using the Hitachi S-3000N variable pressure scanning electron microscopy.

Image analysis

The optical sectioning of the confocal image stacks and cell lengths along different directions were analyzed using Nikon NIS-Elements software. Time-lapse confocal series were processed using MorphoGraphX as described previously (Barbier de Reuille et al., 2015) and as detailed below. The confocal stacks of a flower were converted to TIFF format using FIJI (Schindelin et al., 2012) and subsequently imported into MorphoGraphX. The TIFF image stacks were processed with Gaussian blur and edge detect to extract a solid shape of the flower. Subsequently, the solid shape was loaded with a triangular mesh on its surface using 5 μm cubes. After the mesh was smoothed and subdivided several times to reach ∼200 000 vertices and to have a similar shape as the original stacks, FM4-64 signal was projected perpendicularly onto the extracted surface using a depth of 1–3 μm from the epidermis within the stacks. After sepal cells were manually seeded and segmented, cell lineage in the 12 h time interval was determined manually by matching mother and daughter cell labels. Heatmaps of cell growth rate were produced using the cell lineage map and shown with the ratio of cell area during the 12 h time interval (cell area at the second time point divided by the cell area at the first time point). The resulting values of the heatmap of the cellular growth rate were exported and analyzed in Excel. Cell areas were exported by using the heatmap function in MorphoGraphX and analyzed in Excel.

For the analysis of cell growth anisotropy, after the mother and daughter stacks were processed with fixed corners, the heatmap of cell growth anisotropy was generated using the correspondence of corners between mother and daughter cells and shown with the ratio of cell deformation in the maximal direction to the minimal direction in the 12 h time interval. The resulting values of the heatmap of cell growth anisotropy were exported and analyzed in Excel. Heatmaps of cell growth rate and cell growth anisotropy in the 12 h time interval were displayed on the first time point.

For the analysis of CMT array orientation and anisotropy, the confocal stacks of a sepal were processed in MorphoGraphX to segment the individual cells by using the above procedures, and then the principle orientation and the heatmap of anisotropy of CMT arrays were computed based on a related algorithm in MorphoGraphX. The resulting values of the heatmap of CMT array anisotropy were exported and analyzed in Excel.

The measurement of fluorescence intensity was described previously (Shi et al., 2016).

Immunohistochemistry

The immunofluorescence labeling of demethyl-esterified HG was described previously (Qi et al., 2017) and is detailed below. *Arabidopsis* inflorescence apices were collected and placed in precooled methanol, vacuum infiltrated for 30 min at 4°C, and stored overnight at 4°C. After dehydration, apices were embedded in Steedman's wax composed of PEG 400 distearate and 1-hexadecanol (Sigma-Aldrich). The wax ribbons of 6 μm sections were cut using a Lecia RM2255 microtome. After rehydration, the sections were pretreated for 1 h with 2% (w/v) BSA in T/Ca/S (20 mM Tris–HCl, 1 mM $CaCl_2$, 150 mM NaCl [pH 8.2], for the 2F4 antibody) or PBS (for the LM19 antibody) buffer and incubated overnight with the antibody hybridoma supernatant (PlantProbes) diluted 1:500 in buffer containing 0.1% (w/v) BSA. After three washes in buffer with 0.1% (v/v) Tween 20, sections were incubated for 1 h with secondary Alexa Fluor 546 goat anti-mouse IgG (Thermo Fisher, for the 2F4 antibody) or Alexa Fluor 546 goat anti-rat IgG (Thermo Fisher, for the LM19 antibody), diluted 1:750 in buffer containing 0.1% (w/v) BSA. After additional rinses in buffer with 0.1% (v/v) Tween 20, sections were stained with 1 μg/ml DAPI for 5 min. After three washes in water, sections were mounted in ProLong Antifade (Thermo Fisher) under coverslips and examined using a confocal laser scanning microscope.

AFM

AFM indentation experiments were carried out with a BioScope Catalyst AFM (Bruker) as described previously (Qi et al., 2017). The experimental setup is expected to have limited influence by turgor pressure. PeakForce QNM AFM was used to record surface topology and create an elastic modulus map. All measurements were performed using standard pyramidal silicon nitride probes (SCANASYST-AIR; Bruker) with triangular cantilevers. The probe's tip radius of 2 nm was given by the manufacturer, and its spring constant was around 0.4 N/m. Each probe was calibrated based on a relative calibration method by ∼10 nm indentation on the Bruker's polystyrene test sample (PDMS-SOFT-2 with 3.5 megapascals), in water. The topology and elastic modulus images were collected, based on 10 nm indentation setting, with a size of 20 × 20 μm^2 in cauline leaves and 5 × 5 μm^2 in sepals, and at a resolution of 512 × 512 pixels. A 0.5 Hz scanning rate was used and the Possion's rate was set as 0.5. For our samples, we obtained over 262 144 elastic modulus values for 512 × 512 pixel for each scanned image.

Cauline leaves with a 2 mm width and sepals with a 1 mm width were detached from stems or flowers and then used for the measurement. The abaxial side of cauline leaves and sepals were facing upward and then adhered to a Petri dish using nail polish. All indentation experiments

were carried out in water at room temperature. The data were analyzed using Nanoscope Analysis version 1.8 software and Excel.

Quantification and statistical analysis

For phenotypic quantification (as shown in Figures 1C, 1E, 2B, 2D, 3M, 4D, and 4E), length, width, and area of cauline leaves and sepals were measured using FIJI, the values of length, width, and area were exported and analyzed with Excel to calculate the average length, width, length–width ratio, and area. The resulting data were presented as mean ± SEM, and at least 12 individual cauline leaves or sepals were used for quantification. Statistical analysis was performed using Student's *t*-test in Excel, and *P* values less than 0.05 were considered significantly different for any set of data.

For gene expression analysis via *in situ* hybridization (as shown in Supplemental Figure 1 and Figure 3E, 3G, and 3H), two biological replicates were performed, and each biological replicate was run in at least five plants for antisense probe hybridization and at least two plants for sense probe hybridization. For gene expression analysis via low-melting agarose sectioning (as shown in Figures 1F, 1G, and 3F), at least three independent plants were analyzed. For signal intensity measurement of LM19 and 2F4 (as shown in Figure 6C and Supplemental Figure 4C), at least 12 independent sepals were analyzed with FIJI. Statistical analysis was performed using a Student's *t*-test in Excel, and *P* values less than 0.05 were considered as significantly different for any set of data.

For qRT–PCR analysis (as shown in Figure 3A–3D), at least three independent biological replicates were used for each sample and each biological replicate run in technical triplicate. For transient transfection assays in *Arabidopsis* protoplasts (as shown in Figure 3I), at least three independent biological experiments were performed and each run in technical triplicate. Statistical analysis was performed using a Student's *t*-test in Excel, and *P* values less than 0.05 were considered as significantly different for any set of data.

For quantification of cell lengths of cauline leaves and sepals along proximodistal and mediolateral axes, 200 cells from 10 plants were used for quantification (as shown in Figure 5B, 5D, and 5F). Statistical analysis was performed using a Student's *t*-test in Excel, and *P* values less than 0.05 were considered as significantly different for any set of data. For quantification of cell area, cellular growth rate, and cellular growth anisotropy of sepals (as shown in Figure 5H and 5I), data are displayed in boxplots, and *n* represents the number of cells from three individual plants used for quantification. The details are as follows: Col-0 (n = 112), E1439 (n = 144), and *dwf4-102* (n = 124). Statistical analysis was performed using Student's *t*-test in Excel, and *P* values less than 0.05 were considered significant for any set of data.

SUPPLEMENTAL INFORMATION

Supplemental information is available at Molecular Plant Online.

FUNDING

Y.J. was supported by the National Natural Science Foundation of China (NSFC) grants 31825002 and 31861143021, the Key Research Project of the Frontier Science of CAS grant ZDBS-LY-SM012, and the Strategic Priority Research Program of CAS grant XDA24020203. Y.W. acknowledges the National Key R&D Program of China grant 2019YFA0903902 and NSFC grant 31871245. F.D. was supported by a Young Scientists Fund of NSFC (grant 32000507). C.T. was supported by NSFC grants 31961133010 and 31970805, and the Youth Innovation Promotion Association of CAS (award 2017139).

AUTHOR CONTRIBUTIONS

Conceptualization, Y.W. and Y.J.; experimental investigation, B.W., Y.X., F.D., C.T., and J.H.; computational simulation, L.Z. and X.G.; formal analysis and data curation, Y.X., B.W., F.D., S.L., and M.L.; writing, Y.X., Y.J., L.Z., Y.W., X.G., and F.D.

ACKNOWLEDGMENTS

We thank Olivier Hamant, Wen-Hui Lin, Dolf Weijers, and ABRC for seeds. No conflict of interest declared.

Received: August 12, 2020
Revised: January 13, 2021
Accepted: March 10, 2021
Published: March 11, 2021

REFERENCES

Ali, O., Mirabet, V., Godin, C., and Traas, J. (2014). Physical models of plant development. Annu. Rev. Cell Dev. Biol. **30**:59–78.

Andriankaja, M., Dhondt, S., De Bodt, S., Vanhaeren, H., Coppens, F., De Milde, L., Muhlenbock, P., Skirycz, A., Gonzalez, N., Beemster, G.T., et al. (2012). Exit from proliferation during leaf development in *Arabidopsis thaliana*: a not-so-gradual process. Dev. Cell **22**:64–78.

Azpiroz, R., Wu, Y., LoCascio, J.C., and Feldmann, K.A. (1998). An *Arabidopsis* brassinosteroid-dependent mutant is blocked in cell elongation. Plant Cell **10**:219–230.

Barbier de Reuille, P., Routier-Kierzkowska, A.L., Kierzkowski, D., Bassel, G.W., Schupbach, T., Tauriello, G., Bajpai, N., Strauss, S., Weber, A., Kiss, A., et al. (2015). MorphoGraphX: a platform for quantifying morphogenesis in 4D. eLife **4**:05864.

Belkhadir, Y., Jaillais, Y., Epple, P., Balsemao-Pires, E., Dangl, J.L., and Chory, J. (2012). Brassinosteroids modulate the efficiency of plant immune responses to microbe-associated molecular patterns. Proc. Natl. Acad. Sci. U S A **109**:297–302.

Ben-Gera, H., Shwartz, I., Shao, M.R., Shani, E., Estelle, M., and Ori, N. (2012). *ENTIRE* and *GOBLET* promote leaflet development in tomato by modulating auxin response. Plant J. **70**:903–915.

Bilsborough, G.D., Runions, A., Barkoulas, M., Jenkins, H.W., Hasson, A., Galinha, C., Laufs, P., Hay, A., Prusinkiewicz, P., and Tsiantis, M. (2011). Model for the regulation of *Arabidopsis thaliana* leaf margin development. Proc. Natl. Acad. Sci. U S A **108**:3424–3429.

Boudon, F., Chopard, J., Ali, O., Gilles, B., Hamant, O., Boudaoud, A., Traas, J., and Godin, C. (2015). A computational framework for 3D mechanical modeling of plant morphogenesis with cellular resolution. PLoS Comput. Biol. **11**:e1003950.

Braybrook, S.A., and Peaucelle, A. (2013). Mechano-chemical aspects of organ formation in *Arabidopsis thaliana*: the relationship between auxin and pectin. PLoS One **8**:e57813.

Choe, S., Dilkes, B.P., Fujioka, S., Takatsuto, S., Sakurai, A., and Feldmann, K.A. (1998). The *DWF4* gene of *Arabidopsis* encodes a cytochrome P450 that mediates multiple 22alpha-hydroxylation steps in brassinosteroid biosynthesis. Plant Cell **10**:231–243.

Chung, Y., Maharjan, P.M., Lee, O., Fujioka, S., Jang, S., Kim, B., Takatsuto, S., Tsujimoto, M., Kim, H., Cho, S., et al. (2011). Auxin stimulates *DWARF4* expression and brassinosteroid biosynthesis in *Arabidopsis*. Plant J. **66**:564–578.

Coen, E., Kennaway, R., and Whitewoods, C. (2017). On genes and form. Development **144**:4203–4213.

Das Gupta, M., and Tsiantis, M. (2018). Gene networks and the evolution of plant morphology. Curr. Opin. Plant Biol. **45**:82–87.

De Rybel, B., Vassileva, V., Parizot, B., Demeulenaere, M., Grunewald, W., Audenaert, D., Van Campenhout, J., Overvoorde, P., Jansen, L., Vanneste, S., et al. (2010). A novel aux/IAA28 signaling cascade activates GATA23-dependent specification of lateral root founder cell identity. Curr. Biol. **20**:1697–1706.

Du, F., Guan, C., and Jiao, Y. (2018). Molecular mechanisms of leaf morphogenesis. Mol. Plant **11**:1117–1134.

Feng, F., Yang, F., Rong, W., Wu, X., Zhang, J., Chen, S., He, C., and Zhou, J.M. (2012). A *Xanthomonas* uridine 5'-monophosphate transferase inhibits plant immune kinases. Nature **485**:114–118.

Fox, S., Southam, P., Pantin, F., Kennaway, R., Robinson, S., Castorina, G., Sanchez-Corrales, Y.E., Sablowski, R., Chan, J., Grieneisen, V., et al. (2018). Spatiotemporal coordination of cell division and growth during organ morphogenesis. PLoS Biol. **16**:e2005952.

Gilmour, D., Rembold, M., and Leptin, M. (2017). From morphogen to morphogenesis and back. Nature **541**:311–320.

Goda, H., Sasaki, E., Akiyama, K., Maruyama-Nakashita, A., Nakabayashi, K., Li, W., Ogawa, M., Yamauchi, Y., Preston, J., Aoki, K., et al. (2008). The AtGenExpress hormone and chemical treatment data set: experimental design, data evaluation, model data analysis and data access. Plant J. **55**:526–542.

Guan, C., Wu, B., Yu, T., Wang, Q., Krogan, N.T., Liu, X., and Jiao, Y. (2017). Spatial auxin signaling controls leaf flattening in *Arabidopsis*. Curr. Biol. **27**:2940–2950.

Guilfoyle, T.J., and Hagen, G. (2007). Auxin response factors. Curr. Opin. Plant Biol. **10**:453–460.

Hervieux, N., Dumond, M., Sapala, A., Routier-Kierzkowska, A.L., Kierzkowski, D., Roeder, A.H., Smith, R.S., Boudaoud, A., and Hamant, O. (2016). A mechanical feedback restricts sepal growth and shape in *Arabidopsis*. Curr. Biol. **26**:1019–1028.

Kierzkowski, D., Runions, A., Vuolo, F., Strauss, S., Lymbouridou, R., Routier-Kierzkowska, A.L., Wilson-Sánchez, D., Jenke, H., Galinha, C., Mosca, G., et al. (2019). A growth-based framework for leaf shape development and diversity. Cell **177**:1405–1418.

Krogan, N.T., Ckurshumova, W., Marcos, D., Caragea, A.E., and Berleth, T. (2012). Deletion of MP/ARF5 domains III and IV reveals a requirement for Aux/IAA regulation in *Arabidopsis* leaf vascular patterning. New Phytol. **194**:391–401.

Kuchen, E.E., Fox, S., de Reuille, P.B., Kennaway, R., Bensmihen, S., Avondo, J., Calder, G.M., Southam, P., Robinson, S., Bangham, A., et al. (2012). Generation of leaf shape through early patterns of growth and tissue polarity. Science **335**:1092–1096.

Kutschera, U., and Niklas, K.J. (2007). The epidermal-growth-control theory of stem elongation: an old and a new perspective. J. Plant Physiol. **164**:1395–1409.

Li, J., Nam, K.H., Vafeados, D., and Chory, J. (2001). BIN2, a new brassinosteroid-insensitive locus in *Arabidopsis*. Plant Physiol. **127**:14–22.

Malinowski, R., Kasprzewska, A., and Fleming, A.J. (2011). Targeted manipulation of leaf form via local growth repression. Plant J. **66**:941–952.

Nakamoto, D., Ikeura, A., Asami, T., and Yamamoto, K.T. (2006). Inhibition of brassinosteroid biosynthesis by either a dwarf4 mutation or a brassinosteroid biosynthesis inhibitor rescues defects in tropic responses of hypocotyls in the *Arabidopsis* mutant nonphototropic hypocotyl 4. Plant Physiol. **141**:456–464.

Noguchi, T., Fujioka, S., Choe, S., Takatsuto, S., Yoshida, S., Yuan, H., Feldmann, K.A., and Tax, F.E. (1999). Brassinosteroid-insensitive dwarf mutants of *Arabidopsis* accumulate brassinosteroids. Plant Physiol. **121**:743–752.

Okushima, Y., Overvoorde, P.J., Arima, K., Alonso, J.M., Chan, A., Chang, C., Ecker, J.R., Hughes, B., Lui, A., Nguyen, D., et al. (2005). Functional genomic analysis of the *AUXIN RESPONSE FACTOR* gene family members in *Arabidopsis thaliana*: unique and overlapping functions of *ARF7* and *ARF19*. Plant Cell **17**:444–463.

Paredez, A.R., Somerville, C.R., and Ehrhardt, D.W. (2006). Visualization of cellulose synthase demonstrates functional association with microtubules. Science **312**:1491–1495.

Peaucelle, A., Braybrook, S.A., Le Guillou, L., Bron, E., Kuhlemeier, C., and Hofte, H. (2011). Pectin-induced changes in cell wall mechanics underlie organ initiation in *Arabidopsis*. Curr. Biol. **21**:1720–1726.

Pérez-Pérez, J.M., Ponce, M.R., and Micol, J.L. (2002). The *UCU1 Arabidopsis* gene encodes a SHAGGY/GSK3-like kinase required for cell expansion along the proximodistal axis. Dev. Biol. **242**:161–173.

Qi, J., Wu, B., Feng, S., Lü, S., Guan, C., Zhang, X., Qiu, D., Hu, Y., Zhou, Y., Li, C., et al. (2017). Mechanical regulation of organ asymmetry in leaves. Nat. Plants **3**:724–733.

Rademacher, E.H., Moller, B., Lokerse, A.S., Llavata-Peris, C.I., van den Berg, W., and Weijers, D. (2011). A cellular expression map of the *Arabidopsis AUXIN RESPONSE FACTOR* gene family. Plant J. **68**:597–606.

Reinhardt, B., Hanggi, E., Muller, S., Bauch, M., Wyrzykowska, J., Kerstetter, R., Poethig, S., and Fleming, A.J. (2007). Restoration of *DWF4* expression to the leaf margin of a *dwf4* mutant is sufficient to restore leaf shape but not size: the role of the margin in leaf development. Plant J. **52**:1094–1104.

Reinhardt, D., Mandel, T., and Kuhlemeier, C. (2000). Auxin regulates the initiation and radial position of plant lateral organs. Plant Cell **12**:507–518.

Reinhardt, D., Pesce, E.R., Stieger, P., Mandel, T., Baltensperger, K., Bennett, M., Traas, J., Friml, J., and Kuhlemeier, C. (2003). Regulation of phyllotaxis by polar auxin transport. Nature **426**:255–260.

Roeder, A.H., Tarr, P.T., Tobin, C., Zhang, X., Chickarmane, V., Cunha, A., and Meyerowitz, E.M. (2011). Computational morphodynamics of plants: integrating development over space and time. Nat. Rev. Mol. Cell Biol. **12**:265–273.

Runions, A., Tsiantis, M., and Prusinkiewicz, P. (2017). A common developmental program can produce diverse leaf shapes. New Phytol. **216**:401–418.

Sampathkumar, A., Yan, A., Krupinski, P., and Meyerowitz, E.M. (2014). Physical forces regulate plant development and morphogenesis. Curr. Biol. **24**:R475–R483.

Schindelin, J., Arganda-Carreras, I., Frise, E., Kaynig, V., Longair, M., Pietzsch, T., Preibisch, S., Rueden, C., Saalfeld, S., Schmid, B., et al. (2012). Fiji: an open-source platform for biological-image analysis. Nat. Methods **9**:676–682.

Shi, B., and Vernoux, T. (2019). Patterning at the shoot apical meristem and phyllotaxis. Curr. Top. Dev. Biol. **131**:81–107.

Shi, B., Zhang, C., Tian, C., Wang, J., Wang, Q., Xu, T., Xu, Y., Ohno, C., Sablowski, R., Heisler, M.G., et al. (2016). Two-step regulation of a meristematic cell population acting in shoot branching in *Arabidopsis*. PLoS Genet. **12**:e1006168.

Sun, Y., Zhou, Q., Zhang, W., Fu, Y., and Huang, H. (2002). ASYMMETRIC LEAVES1, an *Arabidopsis* gene that is involved in the control of cell differentiation in leaves. Planta **214**:694–702.

Tian, C., Wang, Y., Yu, H., He, J., Wang, J., Shi, B., Du, Q., Provart, N.J., Meyerowitz, E.M., and Jiao, Y. (2019). A gene expression map of shoot domains reveals regulatory mechanisms. Nat. Commun. **10**:141.

Verhertbruggen, Y., Marcus, S.E., Haeger, A., Ordaz-Ortiz, J.J., and Knox, J.P. (2009). An extended set of monoclonal antibodies to pectic homogalacturonan. Carbohydr. Res. **344**:1858–1862.

Wang, X., Chen, E., Ge, X., Gong, Q., Butt, H., Zhang, C., Yang, Z., Li, F., and Zhang, X. (2018). Overexpressed *BRH1*, a RING finger gene, alters rosette leaf shape in *Arabidopsis thaliana*. Sci. China Life Sci. **61**:79–87.

Wang, X., Wilson, L., and Cosgrove, D.J. (2020). Pectin methylesterase selectively softens the onion epidermal wall yet reduces acid-induced creep. J. Exp. Bot. **71**:2629–2640.

Whitewoods, C.D., and Coen, E. (2017). Growth and development of three-dimensional plant form. Curr. Biol. **27**:R910–R918.

Wolf, S., Mravec, J., Greiner, S., Mouille, G., and Hofte, H. (2012). Plant cell wall homeostasis is mediated by brassinosteroid feedback signaling. Curr. Biol. **22**:1732–1737.

Zhang, Z., Tucker, E., Hermann, M., and Laux, T. (2017). A molecular framework for the embryonic initiation of shoot meristem stem cells. Dev. Cell **40**:264–277.

Zhao, F., Du, F., Oliveri, H., Zhou, L., Ali, O., Chen, W., Feng, S., Wang, Q., Lü, S., Long, M., et al. (2020). Microtubule-mediated wall anisotropy contributes to leaf blade flattening. Curr. Biol. **30**:3972–3985.

Zhao, X., Meng, Z., Wang, Y., Chen, W., Sun, C., Cui, B., Cui, J., Yu, M., Zeng, Z., Guo, S., et al. (2017). Pollen magnetofection for genetic modification with magnetic nanoparticles as gene carriers. Nat. Plants **3**:956–964.

Zhou, L., Du, F., Feng, S., Hu, J., Lu, S., Long, M., and Jiao, Y. (2020). Epidermal restriction confers robustness to organ shapes. J. Integr. Plant Biol. **62**:1853–1867.